Materials Science & Engineering A xxx (xxxx) 146619

Contents lists available at ScienceDirect

Materials Science & Engineering A

journal homepage: www.elsevier.com/locate/msea

Identification of an affordable and printable metastable β Ti alloy with outstanding deformation behaviour for use in laser powder bed fusion

Zhiyi Zou [a, **], Matthew K. Dunstan [b], Brandon McWilliams [b], Richard Hague [a], Marco Simonelli [a, *]

[a] Centre for Additive Manufacturing, University of Nottingham, Nottingham, NG8 1BB, UK
[b] D.E.V.C.O.M. Army Research Laboratory, Aberdeen Proving Ground, Aberdeen, MD, 21005, USA

ARTICLE INFO

Keywords:
Laser powder bed fusion
Metastable β Ti alloys
Material design
Deformation behaviour
Ti-Cr-Sn alloy

ABSTRACT

Research on metastable β Ti alloys has recently shown the possibility to achieve outstanding ductility and work hardening behaviours by engineering the materials' unique strain transformable attributes and responses to heat treatment. As quenching is central to the development of the metastable phase in these alloys, it is of interest to understand how these materials could be designed and developed for use in laser additive manufacturing where feedstocks experience numerous rapid thermal cycles. In this context, we first propose a material design framework to identify printable metastable Ti alloys for laser powder bed fusion (L-PBF). We focus on the ternary Ti-Cr-Sn system for both its affordable character and interest in the biomedical field. The design framework combines criteria based on well-established empirical parameters that we use to compare stability of β phase and resistance to cracking during L-PBF, i.e. its printability. The design work is supported by series of microstructural investigations on arc-melted buttons of selected compositions. Using such methodology we identify Ti-7.5Cr-4.5Sn as strain transformable alloy of good printability and we then characterise this alloy in depth in a series of laser powder bed fusion experiments. Printability of this alloy is further demonstrated via printing experiments using a variety of processing conditions while the deformation character is studied using compressive testing. It was found that the identified Ti-7.5Cr-4.5Sn alloy can achieve a high compressive strain exceeding 70 % thanks to deformation mechanisms that combine dislocation slip and {3 3 2}<1 1 3> twinning. This research paves the way towards the identification of novel Ti alloys for L-PBF beyond those used in the aerospace sector, opening the way for a broader field of applications.

1. Introduction

The development of metal additive manufacturing, especially laser powder bed fusion (L-PBF), has undoubtedly demonstrated an ability to provide unprecedented design freedom, as well as the opportunity to manufacture materials of outstanding properties [1]. In the context of Titanium (Ti) alloys, research has focused extensively on Ti-6Al-4V, and this alloy is often used as a model material [1–3]. However, the intrinsic rapid thermal cycles associated with L-PBF processing cause most Commercial-Off-The-Shelf (COTS) Ti alloys (including Ti-6Al-4V) to form unfavourable microstructural features in the as-printed condition, which are known to undermine tensile and fatigue properties [4,5]. For example, martensite α' is generally obtained in the printed near α Ti alloys or α + β Ti alloys, including Ti-6Al-4V [3,6]. As a brittle phase inherited with high-density crystal defects, the existence of a significant amount of martensite α' typically results in unacceptable ductility of the printed material [5,7].

Recently, various approaches have been proposed to overcome this challenge. Ductility in the as-printed material has been shown to be influenced by the utilisation of specific process parameters that allow the user to impose a desirable heat treatment during the building process (often referred to as "*in-situ* heat treatment") [8–10]. These include the assistance of ultrasound during the process to break down the grain structure anisotropy [11,12] and *ad-hoc* modifications of the COTS material [13–15]. However, post-process heat treatment is generally considered necessary for L-PBF Ti alloys, adding to labour and production costs [16].

Unlike the commonly used near α Ti alloys or α + β Ti alloys, metastable β Ti alloys offer a potential advantage to be directly employed in the as-printed status or after minimal stress relief treatment, as these materials are developed through a quenching treatment, and

* Corresponding author.
** Corresponding author.
E-mail address: Marco.Simonelli@nottingham.ac.uk (M. Simonelli).

https://doi.org/10.1016/j.msea.2024.146619
Received 6 December 2023; Received in revised form 28 March 2024; Accepted 4 May 2024
0921-5093/

therefore are designed with rapid cooling rate conditions in mind [17,18]. The promise offered by these alloys lies in the fact that metastable β phase is typically strain transformable. As such, deformation mechanisms including mechanical twinning (TWIN) and stress-induced martensite formation (TRIP) can take place in addition to slip) and therefore superior ductility can be achieved, at least in principle [17,19,20].

Related supporting research has shown that selected metastable β-Ti alloys can be successfully printed and utilised in the as-printed condition, including COTS alloys such as Ti-5Al-5Mo-5V-3Cr (Ti5553) [21,22], Ti-4.5Ta-4Fe-7.5Nb-6Zr (TTFNZ) [23], Ti-3Al-8V-6Cr-4Mo-4Zr (Ti Beta-C) [24], Ti-12Mo-6Zr-2Fe (TMZF) [25], Ti–8Cr–3Al–5Mo–5V (TB2) [26,27], and *ad-hoc* modified COTS [15,28,29], as well as custom designed alloys [17,18,25,30–32]. There remains, however, a lack of understanding about how to specifically identify suitable alloys for the L-PBF process, particularly for less investigated, so-called "affordable" alloy compositions. While the majority of the successfully printed metastable β-Ti alloys are, in fact, formulated with expensive isomorphous β stabilisers [17,18,23,24,26,27,33], only limited research has been reported on processing of Ti alloys that include cheaper eutectoid β stabilisers (e.g. Cr, Fe, Cu) [34]. As an eutectoid β stabiliser, Cr is a popular option to replace the expensive isomorphous β stabilisers, such as V and Mo, in the low-cost Ti alloy, since alloy composition is a ket factor affecting the alloy cost [35]. Based on the London Metal Exchange and Shanghai Metals Market, on March 2024, for 99 % purity metal, the average market price for Cr is about 8 USD/kg, while V is 155 USD/kg and Mo is 45 USD/kg [36,37].

In this context, this research aims to develop a methodology for identifying cost-efficient metastable Ti alloys for use in L-PBF. The design methodology is applied to a Ti-Cr-Sn ternary system, in which both Cr (8 USD/Kg) and Sn (28 USD/Kg) are affordable alloying elements and biocompatible elements, ensuring the cost-efficiency of the raw materials [38] and also likely bio-compatibility. In the study, we show how the alloy constitution can be designed to tune the stability of the phases that can form in this alloy, as well as the strain transformable characteristics. We then show how the developed framework can be used to select the most promising composition in this ternary system and characterise fully the printed alloy thus identified.

2. Methodology

2.1. Material design framework for the identification of printable metastable Ti alloys

The proposed material design framework aims to evaluate *a-priori* (i) aspects of the printability of the material for use in L-PBF – in particular, the susceptibility to crack formation – and (ii) the expected microstructural phases obtained in the L-PBF as-print condition. For each composition taken into consideration, five parameters are evaluated: these include the molybdenum equivalence (Mo_{eq}), the martensitic start temperature Ms*, the electron-to-atom (e/a) ratio, the average bond order ($\overline{Bo}$) and the energy of the d-orbital ($\overline{Md}$) (these being expressed in the form of $\overline{Bo}$ - $\overline{Md}$ diagram). Mo_{eq} and Ms* are used to provide an indication of both crack susceptibility (i.e. printability) and β stability of each alloy, while the e/a ratio and $\overline{Bo}$ - $\overline{Md}$ diagram are utilised to infer β stability and strain transformability character.

2.1.1. The use of molybdenum equivalents (Mo_{eq}) and the martensitic start temperature Ms* parameters to identify printable alloys

Molybdenum equivalents (Mo_{eq}) and the martensitic start temperature Ms* are two empirical parameters often used to compare Ti alloys. Mo_{eq}, defined via Equation (1), is a widely accepted relationship to compare the amount of β stabiliser in different Ti alloys [39,40].

$$\begin{aligned} Mo_{eq} = {} & 1.0\ (\text{wt.\% Mo}) + 0.67\ (\text{wt.\%V}) \\ & + 0.44\ (\text{wt.\% W}) + 0.28\ (\text{wt. \% Nb}) \\ & + 0.22\ (\text{wt.\% Ta}) + 2.9\ (\text{wt.\% Fe}) \\ & + 1.6\,(\text{wt. \% Cr}) - 1.0\ (\text{wt. \% Al}) \\ & - 0.33\ (\text{wt. \% Sn}) - 0.17\,(\text{wt. \% Zr}) \end{aligned} \qquad \text{Equation 1}$$

It is generally believed that $Mo_{eq} > 10$ is needed to retain full β upon quenching, while $Mo_{eq} > 20$ are thought to produce alloys with stable β phase throughout processing and during deformation [39,40]. However, evidence suggests that some alloy systems can also retain full β at a slightly lower Mo_{eq}, such as Ti–10V–2Fe–3Al (Mo_{eq} = 9.5) [41,42] and Ti–5V–5Mo–1Cr–1Fe–5Al (Mo_{eq} = 8) [43].

In addition, the stability of the β upon quenching can instead be evaluated via the martensitic start temperature Ms* of an alloy. Ms*, estimated via Equation 2, physically represents the temperature at which the spontaneous thermally induced martensitic transformation begins during cooling [[4444]].

$$\begin{aligned} Ms^* = {} & 883 - 150\ (\text{wt. \% Fe}) - 96\,(\text{wt. \% Cr}) \\ & - 49\,(\text{wt. \% Mo}) - 37\,(\text{wt. \% V}) \\ & - 17\,(\text{wt. \% Nb}) - 7\,(\text{wt. \% Zr}) - 7\,(\text{wt. \% Sn}) \\ & + 15\,(\text{wt. \% Al})\ (\text{Temperature in °C}) \end{aligned} \qquad \text{Equation 2}$$

Mo_{eq} and Ms* can therefore be used as alloy design parameters. In respect to alloy's printability, it is desirable to minimise Mo_{eq} as β stabilisers (and eutectoid stabilisers in particular) have a tendency to micro-segregate and increase the solidification range of the alloy, which in turn is thought to increase hot crack susceptibility and other typical defects that can occur during the melt pool solidification [17,45]. However, conversely, it is also of interest to minimise the tendency of Ti alloys to undergo solid phase transformation during thermal cycles; the formation of α' martensite and isothermal ω from β are, in fact, associated with localised lattice strains and the generation of residual stresses, which might favour cold cracking and delamination during the build process [3,22]. As a high Ms* indicates that the α' martensite is likely to be retained in the material upon rapid cooling, an alloy with the minimum $Ms*$ (for any given Mo_{eq} value) is preferable to minimise the formation of cold cracks, which generally associated with an enhanced printability.

These preliminary considerations are broadly corroborated by recent literature on L-PBF. Table 1 summarises typical Mo_{eq} and Ms* values for Ti alloys that retain metastable β in the as-printed condition. A trade-off between Mo_{eq} and Ms* can be noticed, and a region with a higher presence of the reported data can be identified. Such observation is further expressed graphically in Fig. 2 (a) in section 3.1, and the identified preferred region is highlighted by the green dash enclosure. This optimum region, $9 < Mo_{eq} < 12$ and 100 °C < Ms* < 300 °C, can be considered the desirable design space for alloy development, as the alloys in this space are likely to be metastable β alloys with promoted L-PBF printability.

Furthermore, how the alloying elements in the selected Ti-Cr-Sn ternary might influence the formation of isothermal ω was also taken into account. For metastable β alloy, the isothermal ω can be precipitated during low-temperature ageing between 200 °C and 500 °C. As the result of such a diffusional process, it has a composition that significantly deviates from the surrounding β matrix, which leads to a much higher elastic and shear modulus of the isothermal ω [46]. Therefore, a considerable amount of lattice strain will be accumulated at the isothermal ω/β interface. For Ti-Cr and its successor alloys, as high-misfit systems, high elastic strain energy in the crystal will exacerbate the accumulation of localised lattice strain [47]. Hence, the presence of isothermal ω in the as-printed material would make the material much more prone to cold cracking.

An analysis of the literature reveals that a concentration of Sn in excess of 4 wt% suppresses the formation of the isothermal ω phase

Table 1
The value of Mo_{eq}. Ms* and corresponding predominant microstructural features in printable metastable β Ti alloy reported in recent literature.

Nomial composition	Microstructure at room temperature	Mo_{eq}	Ms* (°C)	Reference
Ti-6Al-4V-10Mo	*α + β*	*6.68*	*335*	[49]
*Ti-5.5*Al-*10V-2Fe*	*α + β*	*7*	*295.5*	[15]
*Ti-*25Nb	*α + β*	*7*	*458*	[50]
*Ti-*5Al-*5Mo-5V-1Cr-1Fe*	*α (limited) + β*	*7.85*	*282*	[29]
*Ti-*5Al-*5Mo-5V-3Cr (Ti-5553)*	*α (limited) + β*	*8.15*	*240*	[21,22]
*Ti–*37Nb*–6Sn*	*β*	*8.38*	*212*	[51]
*Ti-*25Nb*-3Zr-3Mo-2Sn*	*β*	*8.83*	*276*	[52]
*Ti-10V-2Fe-*3Al	*β*	*9.5*	*258*	[41,42,53]
*Ti–*5Al*–5V–5Mo–3Cr–0.5 Fe*	*β*	*9.6*	*150*	[28]
*Ti-*35Nb*-7Zr-5Ta*	*β*	*9.71*	*239*	[31]
*Ti-*35Nb*-2Ta-3Zr*	*β*	*9.73*	*267*	[30,54]
*Ti–15Mo–5Zr–*3Al	*β*	*11.15*	*158*	[55]
Ti-27.5Nb-8.5Ta-3.5Mo-2.5Zr-4.5Sn	*β*	*11.16*	*195*	[17,32]
*Ti-*42Nb	*β*	*11.76*	*169*	[56]
Ti-15Mo-3Nb-3Al-0.2Si	*β*	*12.84*	*142*	[57]
*Ti-4.5Ta-4Fe-7.*5Nb*-6Zr (TTFNZ)*	*β (+ ω)*	*13.53*	*122*	[23]
Ti-3Al-8V-6Cr-4Mo-4Zr (Ti Beta-C)	*β*	*14.73*	*−163.05*	[24]
Ti-6Mo-5.5Cr-1Co-0.1C	*β (+ ω)*	*16.5*	*61*	[18]
Ti-12Mo-6Zr-2Fe (TMZF)	*β (+ ω)*	*16.78*	*−47*	[25]
*Ti–8Cr–*3Al*–5Mo–5V (TB2)*	*β*	*18.15*	*−270*	[26,27]
Ti-1Al-8V-5Fe	*β*	*18.86*	*−148*	[58]

[47,48]. Therefore, in principle, one should favour the development of alloys with Sn contents equal to or higher than this critical concentration.

2.1.2. Electron-to-atom ratio

The electron-to-atom (e/a) ratio is another commonly used parameter to assess the β stability in β Ti alloy, with alloys with a high ratio displaying generally higher β stability. A critical value of 4.115 ± 0.002 is usually suggested to differentiate the presence or absence of the martensite phase upon quenching, and therefore it is desirable to identify compositions that are associated with similar ratios [59].

2.1.3. The phase stability diagram

The compositions selected per previous parameters were further screened on the base of the average bond order ($\overline{Bo}$) and the energy of the d-orbital ($\overline{Md}$) phase stability diagram [60,61]. $\overline{Bo}$ represents the covalent bond strength between Ti and each alloy element, while $\overline{Md}$ relates to the elements' electronegativity as well as their metallic radius [62]. It is believed that these two electronic parameters can inform the relative chemical stability of the β phase. The two indexes can be calculated via [60]:

$$\overline{Bo} = \sum_{i=1}^{n} X_i (Bo)_i \quad \text{Equation 3}$$

$$\overline{Md} = \sum_{i=1}^{n} X_i (Md)_i \quad \text{Equation 4}$$

where X_i is the atomic fraction of element i in the alloy, $(Md)_i$ is the d-orbital energy level for element i, and $(Bo)_i$ is the bond order for element i. Each alloy, with its $\overline{Bo}$ and $\overline{Md}$ value, corresponds to a unique point in the diagram describing its deformation character. On this basis, only the alloys with desired deformation characters were considered for further testing.

As a widely adopted criterion for Ti alloy desgin, it is generally believed that, a composition located in the centre of the TWIN/TRIP zone and close to the TWIN/TRIP boundary would lead to favourable ductile performance [20,40,63]. Therefore, the centre area across the TWIN/TRIP boundary in the phase stability diagram is the targeted design space for this study.

2.2. Powder-free testing of the arc melted buttons

Arc melting technique has been widely applied to synthesis and evaluate new alloy composition in small batches [64]. Informed by the analysis detailed in Section 2.1, some isolated alloy compositions were formulated in small experimental buttons (<5 g) by melting high purity elements in a water-cooled copper crucible arc melter. The buttons were melted four times to improve homogeneity via non-consumable tungsten electrode under a protective argon atmosphere.

To emulate the thermal history imposed by L-PBF, the flat surface of the buttons was then fully melted with a Renishaw AM400 system using typical laser parameters for the deposition of Ti-6Al-4V, that is a power of 190 W, scan speed of 1.5 m/s, and hatch space of 75 μm [13]. The area was melted using scan tracks distanced by 75 μm and a bidirectional strategy. The material response to laser irradiation was then studied by examining the microstructures formed in the laser melted layer of the buttons. In addition, a Wilson VH3100 hardness tester was used to place Vickers indents in the laser melted depth with a load of 500g (HV0.5). Localised stress was introduced to the material through the indentation, and then the microstructures adjacent to the indents were studied to identify the deformation character of the alloy and assess its tendency to exhibit strain transformability. Further details related to arc melted button testing can be discussed in Appendix A.

2.3. L-PBF fabrication and post-process heat treatment

Several compositions were further tested in an L-PBF apparatus. The feedstock was prepared by mixing grade 2 CP-Ti powder with a particle size between 15 μm and 45 μm (Carpenter Additive Ltd), pure Cr powder with a particle size smaller than 10 μm (Goodfellow Cambridge Ltd), and pure Sn powder with a particle size smaller than 6 μm (Nanoshel-UK Ltd) as per designed quantities. A LabRAM resonant acoustic mixer was used to mix the powder in a dry atmosphere, and ensured the acquired powder mixture was relatively homogenous at the length scale of hundred micrometres, approximately the length scale of the melt pool during laser melting in our L-PBF experiments [65].

A Renishaw AM400 system with a modulated laser was used to print the prepared feedstocks. The laser power was modulated to deliver a pulsed output, and the scan was processed on a point-by-point basis, which is defined by a pulse length (exposure time) and point distance (distance between exposures). Scan parameters, including pre-defined hatch distance (75 μm), layer thickness (30 μm) and various laser powers (200W–300W) and scan speeds (0.75 m/s to 2 mm/s), were applied to determine the process window and understand the preferable volumetric energy density that would lead to near-fully dense printing. The volumetric energy density (u) can be calculated via [66]:

$$u = \frac{P}{v * d * h} \quad \text{Equation 5}$$

where P is the laser power, v is the scan speed, t is the laser exposure time, d is the distance between hatches, and h is the layer thickness. As a modulated laser was applied, the scan speed is expressed as the point distance (l) over the exposure time (t).

As mixed powder feedstock tends to result in elemental segregation [14,58], to homogenise the element distribution in the printed material, a post-process heat treatment was applied. It is an approach also used by analogous research on titanium alloys that are developed by mixing elemental powders [18,25], which will homogenise the element

distribution while mimicking a microstructure similar to the printing of pre-alloy feedstock.

This post-process heat treatment included a sub-transus solution heat treatment followed by a further β solution and quenching treatment, as schematically shown in Fig. 1. The solution heat treatment was conducted in a conventional furnace with a heating rate of 10 °C/min, a soaking duration of 10 h, and followed by air cooling. The soaking temperature for the solution heat treatment was 100 °C lower than the measured β transus of the material. The β transus is the lowest equilibrium temperature to maintain the entire materials in the β region, which was ascertained by Simultaneous Thermal Analysis (STA) using a TA Instruments TGA-SDTQ600 analyser. For the β-solution treatment, the material was heated to a temperature 50 °C higher than the measured β transus, held for 15 min at that temperature, and water quenched. This will later be referred to as the "solution-quenched" condition. All specimens were sealed in vacuum quartz tubes to avoid oxidation.

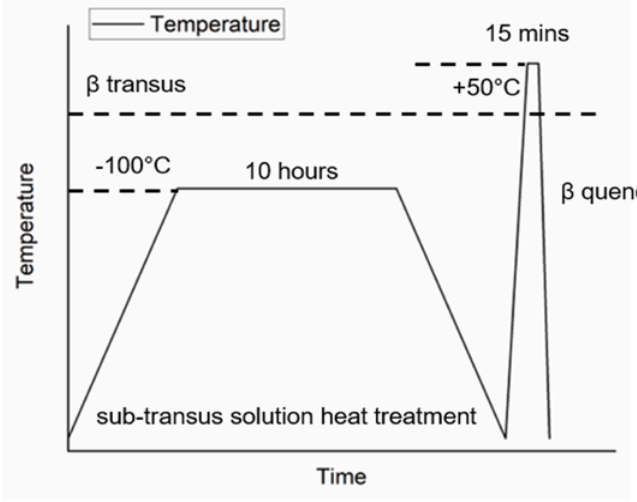

Fig. 1. The schematic shows the heat treatment conducted in this study to homogenise the element distribution in the printed material, consisting of a sub-transus solution heat treatment followed by a further β solution and quenching treatment.

2.4. Microstructural characterisation and mechanical testing

Prior to microstructural characterisation, the samples were mirror-polished following the guidelines stated elsewhere [67]. A final chemical-mechanical polishing with a mixture of 0.03 μm colloidal silica suspension (OP-S) and hydrogen peroxide (H_2O_2, 30 % diluted) on an MD-chem cloth (Struers) was applied. Where needed, the etchant solution of Kroll's reagent was used to reveal microstructure for optical microscopy.

The microstructural constituents of the material under different conditions were examined using X-ray Diffraction (XRD) via a Bruker D8 ADVANCE Cu-Kα1 X-ray source device with the DAVINCI XRD system. The typical microstructural features were observed on the specimen's frontal plane or normal to the build direction (XZ surface, Z direction being the build direction) using a Nikon Optiphot 100 optical microscope and a JEOL 7100F FEG-SEM. The concentration of elements was analysed using Energy-Dispersive X-ray Spectroscopy (EDS) via a JEOL 7100F FEG-SEM at a fixed setting: focus distance of 10 mm, emission energy of 15 kV and probe current of 8. Where needed, the composition was measured at multiple locations, and then the average value was calculated. Furthermore, the crystallographic texture of the specimens was investigated via Electron Back-Scattered Diffraction (EBSD) using a Helios G4 PFIB Xe DualBeam FIB/SEM. Maps were acquired using a step size of 0.2 μm, also from the frontal plane normal to the build direction (XZ surface) of the specimens for consistency. The collected data was analysed using MATLAB toolbox Mtex-5.7.0 and AztecCrystal.

To examine the strain transformability of the printed alloy, the homogenisation heat treated printed cylinders with the dimension of Φ 5 mm and height 10 mm were compressively tested, and the obtained strained microstructure was then analysed. The compression tests were conducted at room temperature on an Instron 5969 with a displacement rate of 0.1 mm/min. The specimens were continuously compressed until they broke or reached the maximum nominal load of 250 kN of the testing apparatus.

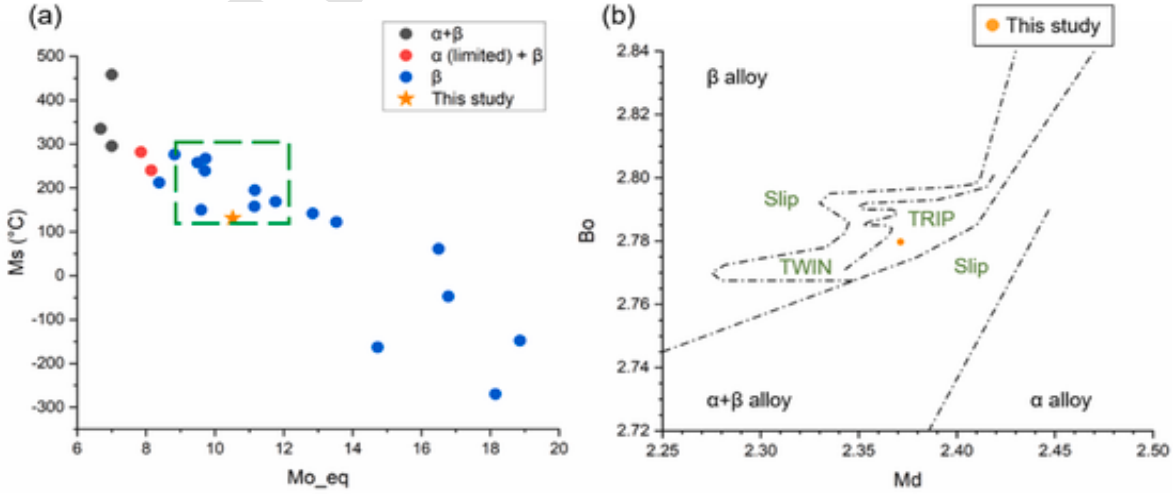

Fig. 2. The nominal composition of Ti-7.5Cr-4.5Sn is selected for this study: (a) recent L-PBF printable metastable β Ti alloy reported in the literature (Table 1) plotted in a Mo_{eq} and Ms*graph with coloured dots. The identified desirable design space is highlighted by the green dashed enclosure, which is used as a guide for this study. The corresponding Mo_{eq} and Ms* of the selected composition plotted via star mark, showing its correlation to the preferable design space; (b) the location of the selected composition in the empirical $\overline{Bo}$ - $\overline{Md}$ diagram. (For interpretation of the references to colour in this figure legend, the reader is referred to the Web version of this article.)

3. Results

3.1. Isolation of alloy from the Ti-Cr-Sn system

After examining the microstructure of several Ti-Cr-Sn alloys in the laser irradiated portion of the buttons (Appendix B) it was concluded that, for this particular ternary system, Mo_{eq} smaller than 10 would result in the presence of a two-phase microstructure regardless of values calculated for Ms*. As expected, these preliminary tests showed that higher Mo_{eq} values help to stabilise the β phase. To maximise printability, it was then considered what the lowest combination of Mo_{eq} and Ms* values that enable retention of a single β microstructure. Results show that in the presently examined ternary, Mo_{eq} ~10.5 combined with a Ms* < 150 °C satisfy this requirement. Mo_{eq} ~10.5 and Ms* < 150 °C were then used as the first criteria to screen the ternary Ti-Cr-Sn system. Using a compositional step size of 0.1 wt% and a maximum threshold of total alloy element concentration of 16 wt%, 149 distinct alloys are found to satisfy the first criteria. A step size of 0.1 wt% can effectively differentiate a wide variety of element concentrations while ensuring a manageable number of options. Meanwhile, a total alloy element concentration higher than 16 wt% would likely make the alloy unworkable for the Ti-Cr-Sn system [68].

The deformation characteristic of the Ti-Cr-Sn compositions for which Mo_{eq} ~10.5 and Ms* < 150 °C are satisfied is then evaluated as per section 2.1.2 and 2.1.3. Favourable composition would locate in the centre of the strain transformable region in the phase stability diagram, right at the TWIP and TRIP boundary or close to it, to enhance ductility aspects [63] and increase alloy solute tolerance to strain transformability.

Based on all the above considerations, a Cr concentration of 7.5 ± 0.3 wt% and an Sn concentration of 4.5 ± 0.4 wt% was found to be a desirable composition. Therefore, the nominal composition of Ti-7.5Cr-4.5Sn was selected for further evaluation.

The selected composition has a corresponding Mo_{eq} of 10.51 and Ms* of 131 °C, e/a ratio of 4.15, located in the design space suggested in section 2.1.1, as plotted in Fig. 2 (a). Its deformation character is further marked in the empirical $\overline{Bo}$ - $\overline{Md}$ diagram, as shown in Fig. 2 (b). The selected Ti-7.5Cr-4.5Sn is located right in the middle of the stain-transformable region traced by $\overline{Bo}$ - $\overline{Md}$ diagram, next to the TWIP and TRIP boundary, a deformation character favoured for this study.

3.2. Microstructure and deformation of laser irradiated Ti-7.5Cr-4.5Sn buttons

The microstructure of the laser irradiated then Vickers indented Ti-7.5Cr-4.5Sn buttons is presented in Fig. 3. The laser melt pool boundary, which distinguishes the laser irradiated region from the original arc melted alloy, can be clearly identified in the forward-scatter images, and is indicated by the blue dashed line plotted in Fig. 3 (a). EBSD scans reveal that the retained material after the laser irradiation and rapid cooling presents a full β microstructure, as shown in Fig. 3 (b), indicating that the β phase is stable throughout the thermal cycles imposed by the rastering lasers. The composition within the laser irradiated region as measured via EDS is reported in Table 2. The experimentally measured concentration of the elements corresponds well with the designed nominal values.

In addition, deformation induced microstructural features can be observed around the Vickers indentation (Fig. 3 (a)), including slip bands (indicated by the white arrow) and twins (indicated by the orange arrow). The relationship between the parent crystal and twins can be further identified through the IPF orientation map, as shown in Fig. 3 (c). It can be concluded that the {3 3 2}<1 1 3> twinning system has

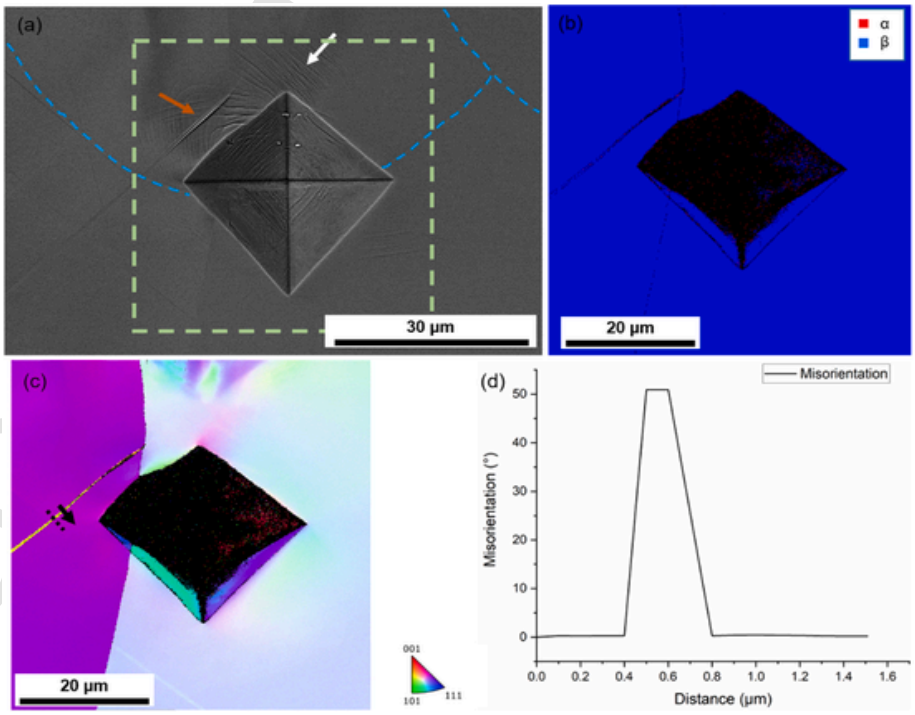

Fig. 3. Typical microstructure of Ti-7.5Cr-4.5Sn laser irradiated buttons. The micrographs also include a hardness indentation to analyse the expected deformation behaviour; (a) secondary electron micrograph revealing microstructural features and heat affected zone (the laser melt pool boundary is plotted by blue dashed lines). Slip bands are indicated by the white arrow, and the orange arrow indicates a deformation twin; the area enclosed in the green dashed box in (a) was further analysed in (b), which shows a phase map and (c) Z-IPF β-an orientation map near the indent. The cumulative misorientation along the black arrow and black dash-line in (c) is reported in (d) and shows a typical strain induced twin in the metastable β phase. (For interpretation of the references to colour in this figure legend, the reader is referred to the Web version of this article.)

Table 2
The average composition within the laser irradiated region of the button measured via EDS.

	Ti	Cr	Sn
Wt%	Bal.	7.43 ± 0.17	4.68 ± 0.19

been activated during the deformation, as evidenced by the misorientation of 50.57° around <1 1 0> between the host β and the identified twin (Fig. 3 (d)) [69]. Thus it can be concluded that Ti-7.5Cr-4.5Sn can retain a full metastable β microstructure despite the thermal cycles imposed upon it by the rastering laser (cycles that are analogous to those of L-PBF). The composition is also, as predicted, strain transformable, with the dominant deformation mechanism including dislocation slip and twinning.

3.3. Printability of the Ti-7.5Cr-4.5Sn and as-printed microstructure

The powder mixture of nominal Ti-7.5Cr-4.5Sn alloy was found to display a good processing range, as it can be printed with near full density (>99.5 %) using a range of acceptable volumetric energy density (VED) (from 53 J/mm3 to 75 J/mm^3). By contrast, powder mixtures with formulations that deviated from the isolated composition, for example, Ti-8.5Cr-4.5Sn and Ti-7.5Cr-2.0Sn, were found challenging to be processed via L-PBF due to cracking issues (details can be accessed via Appendix C).

The relative density of the printed material was estimated via the area percentage of porosity in micrographs of the sectioned and then polished surface. However, elemental segregation was observed in all as-printed samples, as evidenced by a dark contrast in the optical micrographs, as shown in Fig. 4. The microstructural constituents of samples printed using different parameters are presented in Fig. 5. XRD analysis suggests that, as anticipated, the microstructure of the printed material is dominated by the single β phase regardless of the applied process parameters. A limited amount of α phase is also detected in the as-printed material, which can be attributed to the elemental segregation observed in Fig. 4; this was not observed in the laser irradiated buttons, where alloy constituents are highly homogenised.

Based on the print trials, the L-PBF Ti-7.5Cr-4.5Sn hereafter were printed using the following optimised process parameters: laser power of 200W, scan speed of 1.33 m/s and VED of 66.89/mm^3 (Fig. 4 (C)). More details of the as-printed microstructure can be accessed via Appendix D.

3.4. Microstructure of the solution-quenched L-PBF Ti-7.5Cr-4.5Sn before and after compressive deformation

To improve chemical homogeneity, post-processing heat treatments were deemed necessary. The homogenised then solution-quenched microstructure of L-PBF Ti-7.5Cr-4.5Sn is shown in Fig. 6(a). The β grains exhibit a mixed morphology of large columnar and relatively small quasi-equiaxed grains, as shown in Fig. 6. The large columnar grains grow in a direction parallel to the build direction, resulting from the directional cooling of L-PBF [3]. The observed relatively small quasi-equiaxed grain might relate to the localised concentration of alloy elements [13], similar to the elemental segregation revealed in Fig. 4, which provides additional nucleation sites during the L-PBF process. Overall, the β grains size appear similar to that of the L-PBF of pre-alloyed Ti-7.5Cr-4.5Sn. XRD analysis in Fig. 6(b) suggests that a single β microstructure has been retained after homogenisation, with limited residual α. Although the post-process heat treatment has significantly improved homogenisation, a notable amount of elemental segregation can still be observed in Fig. 6 (a), which might contribute to the residual α peaks in the XRD pattern (Fig. 6 (b)). Grain boundary α, a microstructural feature commonly retained in α + β Ti and near β Ti alloys [15,29], is not observed in the homogenised material, as evidenced in Fig. 6 (c).

The composition of the homogenised β grains has been measured by EDS at multiple locations, as well as via ICP-OES, and the average value is reported in Table 3. Compared to the composition measured in the

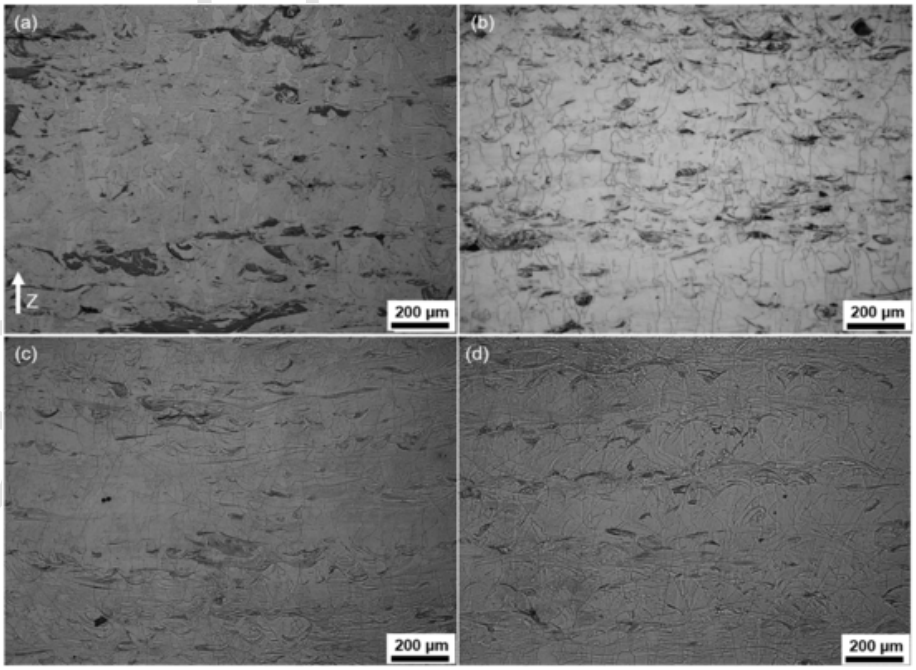

Fig. 4. Optical micrographs showing typical microstructures of Ti-7.5Cr-4.5Sn printed via various process parameters that allowed achieving of high density. Build direction Z is indicated via the white arrow. These microstructures are obtained using (a) laser power of 200W, scan speed of 1.56 m/s, VED of 56.82J/mm^3, (b) laser power of 300W, scan speed of 2.08 m/s, VED of 64.10J/mm^3, (c) laser power of 200W, scan speed of 1.33 m/s, VED of 66.89/mm^3, (d) laser power of 300W, scan speed of 1.88 m/s, VED of 71.01J/mm.^{3}.

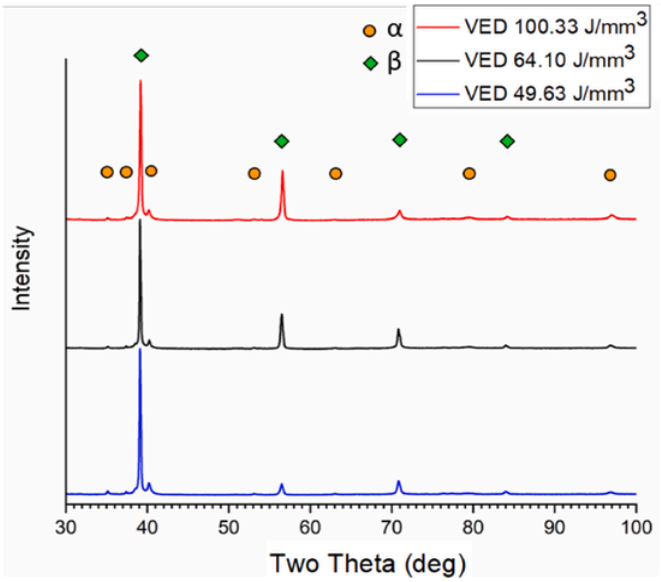

Fig. 5. Phase identified by XRD in Ti-7.5Cr-4.5Sn printed using a range of volumetric energy densities.

buttons (Table 2), a noticeable loss in Cr can be observed. The reasons for such a phenomenon will be further discussed in section 4.2. Despite the Cr losses, for clarity and consistency, the L-PBF material hereafter will still be named following its nominal value (i.e. Ti-7.5Cr-4.5Sn).

The scatter in the EDS analysis listed in Table 3, indicates that the elemental distribution is less homogenised than buttons. This can be attributed to the fact that the as-printed material was soaked at a temperature lower than the β transus to avoid extensive β grain growth. In such case, the diffusion of the segregated alloy element is hindered by both the phase boundary and grain boundary, hindering an effective elemental homogenisation [70].

Samples were then subjected to compressive deformation to assess the dominant deformation mechanism. Results are shown in Fig. 7. An analysis of the microstructure post-compressive test shows a highly deformed grain structure (the grains appear squashed by the compressive load) and a single β phase, as evidenced in Fig. 7 (a) and (b). The lack of additional phases (confirmed by both XRD and EBSD), suggests the absence of TRIP effects. Slip bands and twins can be clearly observed in the Z-IPF orientation map (Fig. 7 (c)) and band contrast images (Fig. 7 (d)). The former microstructural feature has been indicated via black arrows, while the latter has been indicated through the twin-grain boundary plotted in red. EBSD analysis shows evident {3 3 2}<1 1 3> twinning activity and abundant slip systems, which correspond well to the deformation of the button investigated in Fig. 3. It is generally believed that the {3 3 2}<1 1 3> twinning is the most favourable twinning mode in metastable β Ti, as it requires the lowest magnitude of twinning shear and results in the lowest complexity of atomic shuffle [71]. Other twinning systems, including the $\{112\}\langle\bar{1}\bar{1}1\rangle$ twinning, although a major twinning mode for stable body-centred-cubic structure, was not observed in the deformed material.

3.5. Compressive stress-strain curves of the solution-quenched L-PBF Ti-7.5Cr-4.5Sn

The obtained stress-strain curves from the conducted compressive tests are plotted in Fig. 8. The curves are typical of the compressive behaviour of ductile strain transformable metastable Ti alloys [47,72,73]. The homogenised and solution-quenched L-PBF Ti-7.5Cr-4.5Sn achieved a high compressive strain of ~70 % (when the tests stopped at the max load of the equipment), equivalent to the compressive stress of around 5 GPa. All the test specimens showed no observable cracking.

The stress-strain curves suggest that the deformation process consists of three different stages, as illustrated via green dashed lines in Fig. 8. The first stage, stage I, starting from the strain of 0 % to around 8 %,

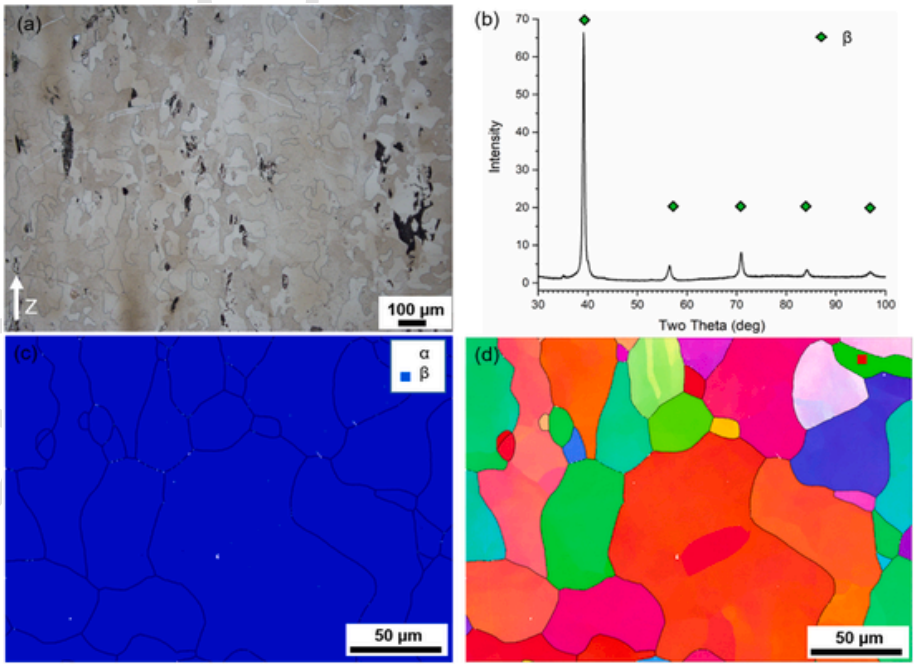

Fig. 6. The microstructure of the homogenied and solution-quenched L-PBF Ti-7.5Cr-4.5Sn prior to compressive deformation, where build direction Z is indicated via the white arrow: (a) optical micrograph showing the morphology of single β microstructure; (b) XRD spectrum showing the microstructural constituents of the material; (c) EBSD phase map further evidence the absence of α phase in the microstructure; (d) Z-IPF β-orientation map showing the typical crystallographic texture of the alloy prior to testing.

Table 3
The average composition of the homogenised and solution-quenched L-PBF Ti-7.5Cr-4.5Sn.

Wt%	Ti	Cr	Sn
EDS	Bal.	7.02 ± 0.29	4.49 ± 0.37
ICP-OES	Bal.	6.88 ± 0.07	4.43 ± 0.04

is the initial elastic deformation and yielding, a common deformation stage for most metallic materials [73]. A compressive modulus of 19.81 ± 0.40 GPa has been recorded for this stage. The small standard deviation value suggests a consistent deformation across different tests. Stage II, starting from the strain of around 8 %–38 %, is observed as a progressively work-hardening stage, with stress-strain curves exhibiting a consistent slope rate, suggesting the operation of one dominant deformation mechanism [74,75]. Finally, stage III, starting from the strain of around 38 % till the end of the test, presents a clear second yielding, suggesting the activation of alternative deformation mechanisms under high stress and strain [72,76].

4. Discussion

4.1. β stability of the obtained L-PBF material and analysis of the deformation behaviour

Despite the considerable loss of Cr during L-PBF (measured at 7 wt% of Cr post build, instead of the nominal 7.5 wt%) the samples retain a full β microstructure. Prior studies have suggested that, for the Ti-Cr binary system, a minimum of approximately 6.5 wt% Cr is required to retain full β upon quenching [39]. Similarly, it is noted that Sn (generally considered a neutral element) has also been reported to have a tendency to stabilise the β phase [77]. Therefore, it is not surprising to observe that the samples homogenised and solution-quenched consist of a full β microstructure. This is also corroborated by research on other Ti-Cr-Sn ternaries, where it is shown that a concentration of 6 wt% Cr with 3 wt% Sn is enough to retain full β upon quenching [78].

A twinning and slip combined deformation mechanism has been identified for the L-PBF Ti-7.5Cr-4.5Sn, with multiple different deformation stages. To better understand the development of deformation behaviour, the evolution of the microstructure is investigated at a strain of 33 % (end of stage II), as shown in Fig. 9.

A single β microstructure has been observed in the 33 % strained material, without any noticeable additional phase (Fig. 9(b)). A significant amount of dislocations can be noted in the obtained microstructure without any noticeable twinning, as demonstrated in Fig. 9 (c) and (d). Therefore, the formation and movement of dislocation under deformation can be considered the primary deformation behaviour in this stage, defining the observed work-hardening exhibited by the material. Preliminary twinning sites can be identified in the deformed microstructure as sub-grains indicated by purple circles in Fig. 9 (c).

This suggests that the β phase in the L-PBF material is relatively stable, and twinning can only be activated under relatively high strain.

Fig. 10, corresponding to a sample strained at 73 %, shows a high density of twins. Both primary and secondary twinning can be identified in the microstructure, as red and blue arrows highlighted in Fig. 10 (b) - secondary twinning being twins produced within the previously formed twinned grains [72,75,79]. Additionally, the propagation of twin boundaries into the adjacent grain has also been observed, as highlighted via yellow arrows in Fig. 10 (b). The migration of twin boundaries results from dislocation movement, and results in the rotation of the sub-grains in the adjacent grain [72,80], as evidenced in the Z-IPF β-orientation map (Fig. 10 (a)). Therefore, such propagation and migration might result in the formation of twinning in the adjacent grain [72].

The activation and proliferation of twins are likely to cause the formation of a second yield in the deformation stage III. It is believed that the formation of twins can suppress the nucleation and growth of cracking, which helps to achieve high stress and strain for the material [24].

In the proposed material design framework, the $\overline{Bo}$ - $\overline{Md}$ diagram is used to predict the deformation mechanism of the selected composition. As a widely used design tool for metastable β alloy, the $\overline{Bo}$ - $\overline{Md}$ diagram is a simplified empirical model which neglects the influence of interstitial elements and impurities in the alloy [81]. As a result, its predicted deformation mechanism deviates from what is observed in the printed material. Such deviation acknowledges the need for the proposed arc melted button study, where the influence of interstitial ele-

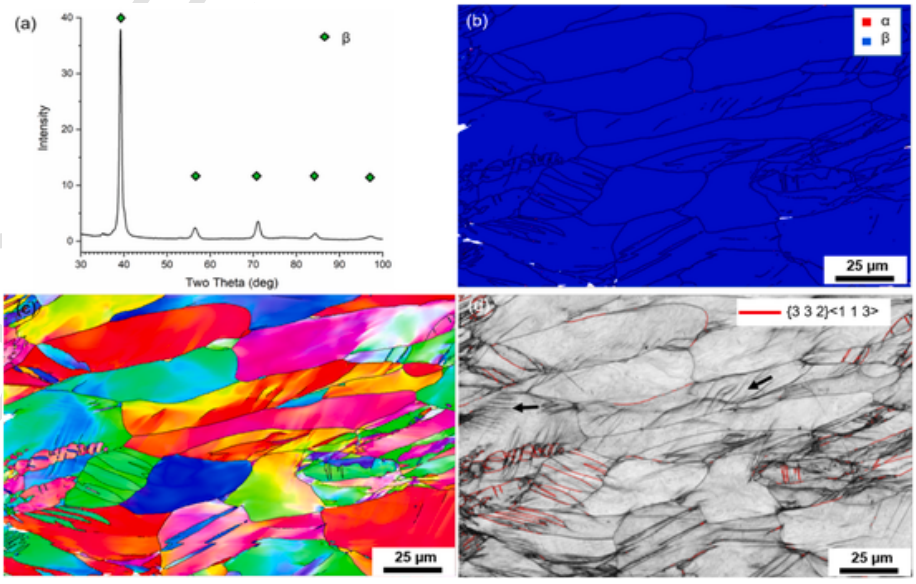

Fig. 7. The microstructure of the homogenised material after compressive testing: (a) microstructural constituents of the material, determined by XRD; (b) EBSD phase map showing retention of single β phase; (c) z-IPF β-orientation map showing the typical highly deformed texture, with the presence of a significant amount of deformation features; (d) band contrast micrograph revealing further details of slip bands (black arrows) and {3 3 2}<1 1 3> twin. The twin grain boundaries are plotted in red. (For interpretation of the references to colour in this figure legend, the reader is referred to the Web version of this article.)

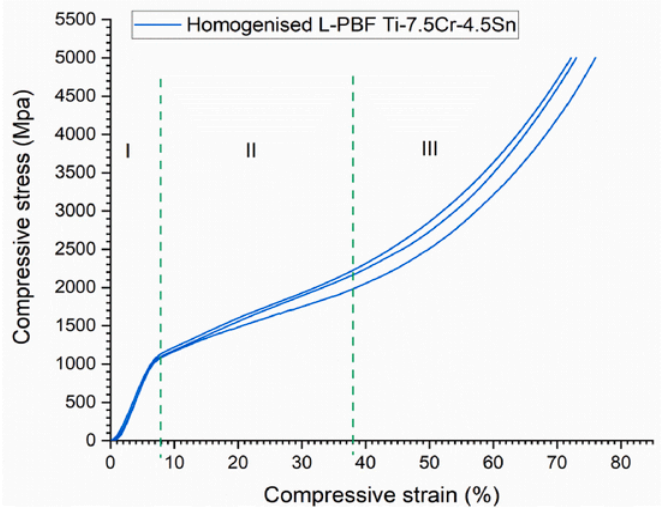

Fig. 8. Compressive stress-strain curves of the homogenised and solution-quenched L-PBF Ti-7.5Cr-4.5Sn. The stress-strain curves suggest that the deformation process can be considered in three different stages, as indicated via green dashed lines. (For interpretation of the references to colour in this figure legend, the reader is referred to the Web version of this article.)

ments and impurities in the alloy has been examined. It can be noticed that the deformation mechanism observed in the printed material matches well with the arc melted button study. Therefore, the proposed arc melted button study can be considered a reliable method to further examine the composition selected through theoretical calculations.

4.2. Variation in element concentration after the L-PBF processing

It is noteworthy that a notable Cr loss in the material was observed after L-PBF printing. Such discrepancy can be partially attributed to the feedstock obtained from elemental powders, resulting in the elemental segregation discussed in section 3.4. Furthermore, the variation in element concentration after printing has also been widely observed for many pre-alloyed feedstocks, and it is mainly attributed to elemental evaporation from the L-PBF melt pool surface [82,83]. Since the typical L-PBF melt pool temperature is significantly higher than the melting temperature of the elements in the alloy [84], elements are likely to evaporate at the melting surface.

The tendency for evaporation between different elements can be compared through their vapour pressure, which is the minimum pressure needed to maintain the element in its liquid phase at the corresponding temperature [85]. In particular, higher vapour pressure indicates a higher tendency to vapourisation. The vapour pressure for individual elements can be calculated using the empirical Antoine equation, as shown below [85]:

$$\log_{10} P = A - B/(T + C) \qquad \text{Equation 6}$$

where P is the vapour pressure in mmHg, T is the temperature in ˚C and A/B/C are component-specific constants (Antoine coefficients) that can be acquired from Ref. [85]. The value of these constants for Ti, Cr and Sn are listed in Table 4.

With the typical melt pool temperatures of Ti alloys in analogous printing conditions are estimated to range between 1700 ˚C and 3250 ˚C [82], the vapour pressure of Ti, Cr and Sn can be calculated (Fig. 11). It can be noted that, Cr not only has the lowest boiling temperature, but also has a vapour pressure significantly higher than the other two elements. Therefore, Cr has the highest potential for evaporation in the Ti-Cr-Sn ternary system, explaining the observed Cr loss after the L-PBF process. It should be noted that due to the relatively high vapour pressure, selective evaporation of Cr has also been reported in the welding of Cr alloyed steels [86]. In similar cases, Al also has a relatively high vapour pressure, Al loss has been widely reported in the L-PBF Ti-6Al-4V [82,83,87].

The material design framework applied in this study is unable to predict the variation in element concentration after L-PBF processing, particularly the observed Cr loss due to selective element evaporation. The selective element evaporation is commonly seen in L-PBF processed materials, resulting in the retained composition deviating from its nominal value [82]. For metastable Ti alloy, the obtained deformation mechanism highly depends on its composition, and the deviation in the retained composition could lead to inferior properties [20,40]. Therefore, predicting element evaporation is helpful for the future material design framework. Recent research suggests that such a prediction can be made by calculating the evaporation thermodynamic and evaporation kinetics of the alloy system [83,87].

5. Conclusion

This study proposes a material design framework for identifying a cost-efficient metastable Ti alloy for L-PBF. The methodology is applied to a Ti-Cr-Sn ternary system. We demonstrate that the composition isolated following this method can retain a desirable metastable Ti alloy with good L-PBF printability and strain transformable characteristics. The results suggest the identified alloy can be a promising structural material used in general land-based applications operating at room temperature or low temperatures (< 200 ˚C), such as unmanned aerial or ground-based vehicle systems, lightweight protective panels, etc. Moreover, we believe the biocompatibility of both Ti, Cr, and Sn offers potential for this alloy to be used in biomedical applications.

From the present study, the following conclusions can be drawn:

- Five parameters, including the Molybdenum equivalence (Mo_{eq}), the martensitic start temperature Ms*, the electron-to-atom (e/a) ratio, the average bond order ($\overline{Bo}$) and the energy of the d-orbital ($\overline{Md}$) are shown to be useful in designing printable and strain transformable Ti alloys.
- The nominal composition of Ti-7.5Cr-4.5Sn has been selected for the study. Experiments on laser surface melting of arc melted buttons suggest that this composition can retain a full β microstructure upon thermal cycles typical for L-PBF. Twins and slip bands are visible around hardness indentations.
- Mixing elemental powders allows the processing of an alloy with a nominal composition of: Ti-7.5Cr-4.5Sn. Printing trials show good printability. A notable Cr loss was observed in the printed samples.
- The homogenised and solution quenched L-PBF Ti-7.5Cr-4.5Sn achieved a high compressive strain exceeding 70 %.
- Such large deformation is supported by three different mechanisms. After the initial yielding, the material experiences a progressively work-hardening stage, where slip is the dominant deformation mechanism. {3 3 2}<1 1 3> twinning system can be activated under relatively high strain, which will result in the progress of second yielding.

CRediT authorship contribution statement

Zhiyi Zou: Writing – original draft, Methodology, Investigation, Formal analysis, Conceptualization. **Matthew K. Dunstan:** Conceptualization, Formal analysis, Writing – review & editing. **Brandon McWilliams:** Conceptualization, Formal analysis, Writing – review & editing. **Richard Hague:** Resources, Writing – review & editing. **Marco Simonelli:** Conceptualization, Formal analysis, Methodology, Resources, Writing – review & editing.

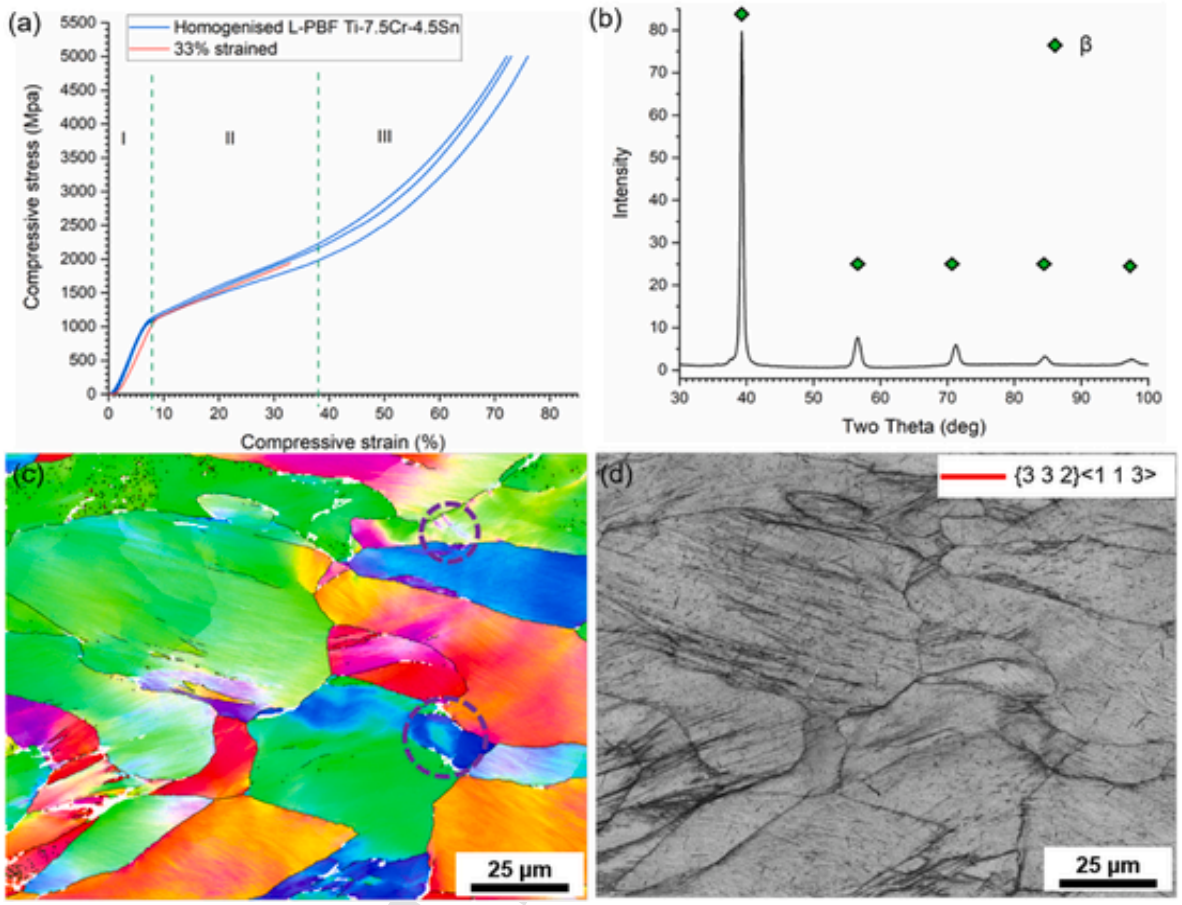

Fig. 9. The dominant deformation mechanism during the work-hardening state of the compressive test is studied in more detail: (a) shows the stress-strain curves of the interrupted test (red curve); (b) shows the microstructural constituents of the material, determined by XRD; (c) Z-IPF β-orientation map showing a deformed texture, with clear presence of deformation features, purple circles highlight the potential nucleation site for twinning; (d) band contrast micrograph revealing a significant amount of dislocations and the absence of twinning at this stage. (For interpretation of the references to colour in this figure legend, the reader is referred to the Web version of this article.)

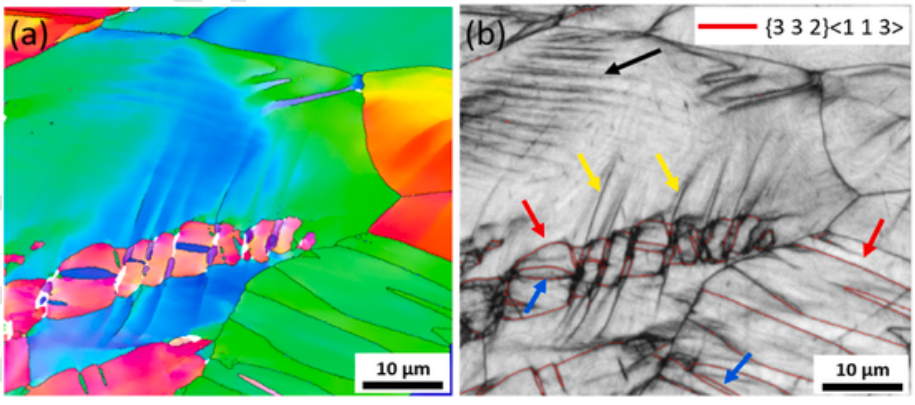

Fig. 10. Micrograph showing the high presence of twins in the compressively deformed L-PBF material: (a) Z-IPF β-orientation map showing the highly deformed texture, with clear presence of deformation features including twins; (b) band contrast image further reveals the details of deformation features, where {3 3 2}<1 1 3> twin boundary is plotted via red line, slip band is indicated by black arrows. Deformation features of primary twinning are indicated by red arrows, while secondary twin features are indicated by blue arrows. The sites where migration of twin boundaries take place are indicated by yellows arrows. (For interpretation of the references to colour in this figure legend, the reader is referred to the Web version of this article.)

Table 4
Value of component-specific Antoine coefficients for Ti, Cr and Sn [85].

	A	B	C
Ti	8.90223	20948.9918	190.76
Cr	8.48706	15307.9218	59.51
Sn	8.54915	16655.8123	336.40

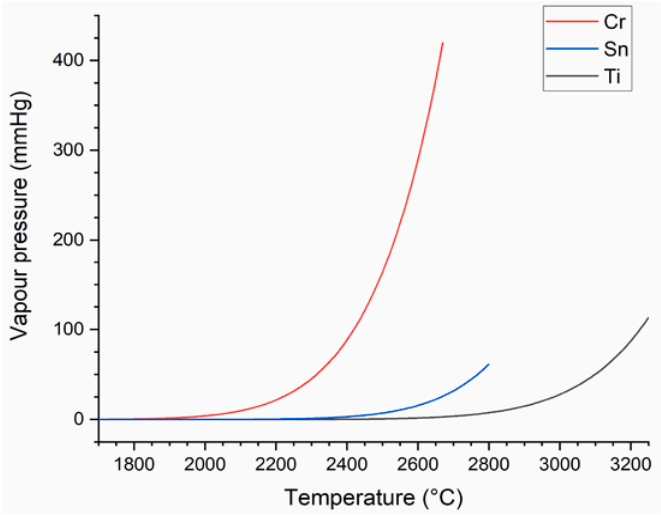

Fig. 11. The calculated vapour pressure of Ti, Cr and Sn at typical melt pool temperatures of Ti alloys printed in with similar laser parameters [84,85].

Declaration of competing interest

The authors declare that they have no known competing financial interests or personal relationships that could have appeared to influence the work reported in this paper.

Data availability

Data will be made available on request.

Acknowledgements

The work presented here has been made possible by funding supported by the U.S.A. Army Research Office (grant W911NF2120202) and Engineering and Physical Sciences Research Council (EPSRC), UK (grant EP/P031684/1). Special thanks to Stuart Robertson (Loughborough University) for his help with the EBSD investigations. The authors acknowledge use of facilities within the Loughborough Materials Characterisation Centre and for access to the Helios PFIB, funded by the EPSRC grant EP/P030599/1.

Appendix A. Supplementary data

Supplementary data to this article can be found online at https://doi.org/10.1016/j.msea.2024.146619.

References

[1] A.M. Beese, B.E. Carroll, Review of mechanical properties of Ti-6Al-4V made by laser-based additive manufacturing using powder feedstock, J. Occup. Med. 68 (3) (2016) 724–734.
[2] Z. Zou, M. Simonelli, J. Katrib, G. Dimitrakis, R. Hague, Refinement of the grain structure of additive manufactured titanium alloys via epitaxial recrystallization enabled by rapid heat treatment, Scripta Mater. 180 (2020) 66–70.
[3] Z. Zou, M. Simonelli, J. Katrib, G. Dimitrakis, R. Hague, Microstructure and tensile properties of additive manufactured Ti-6Al-4V with refined prior-β grain structure obtained by rapid heat treatment, Mater. Sci. Eng., A 814 (2021) 141271.
[4] S. Zhang, Y. Zhang, Z. Zou, Y. Shi, Y. Zang, The microstructure and tensile properties of additively manufactured Ti–6Al–2Zr–1Mo–1V with a trimodal microstructure obtained by multiple annealing heat treatment, Mater. Sci. Eng., A 831 (2022) 142241.
[5] X.-Y. Zhang, G. Fang, S. Leeflang, A.J. Böttger, A. Zadpoor, J. Zhou, Effect of subtransus heat treatment on the microstructure and mechanical properties of additively manufactured Ti-6Al-4V alloy, J. Alloys Compd. 735 (2018) 1562–1575.
[6] Y. Zhang, S. Zhang, Z. Zou, Y. Shi, Achieving an ideal combination of strength and plasticity in additive manufactured Ti–6.5Al–2Zr–1Mo–1V alloy through the development of tri-modal microstructure, Mater. Sci. Eng., A 840 (2022) 142944.
[7] B. Vrancken, L. Thijs, J.-P. Kruth, J. Van Humbeeck, Heat treatment of Ti6Al4V produced by selective laser melting: microstructure and mechanical properties, J. Alloys Compd. 541 (2012) 177–185.
[8] W. Xu, M. Brandt, S. Sun, J. Elambasseril, Q. Liu, K. Latham, K. Xia, M. Qian, Additive manufacturing of strong and ductile Ti–6Al–4V by selective laser melting via in situ martensite decomposition, Acta Mater. 85 (2015) 74–84.
[9] P. Barriobero-Vila, J. Gussone, J. Haubrich, S. Sandlöbes, J.C. Da Silva, P. Cloetens, N. Schell, G. Requena, Inducing stable α + β microstructures during selective laser melting of Ti-6Al-4V using intensified intrinsic heat treatments, Materials 10 (3) (2017).
[10] W. Xu, E.W. Lui, A. Pateras, M. Qian, M. Brandt, In situ tailoring microstructure in additively manufactured Ti-6Al-4V for superior mechanical performance, Acta Mater. 125 (2017) 390–400.
[11] C.J. Todaro, M.A. Easton, D. Qiu, D. Zhang, M.J. Bermingham, E.W. Lui, M. Brandt, D.H. StJohn, M. Qian, Grain structure control during metal 3D printing by high-intensity ultrasound, Nat. Commun. 11 (1) (2020) 142.
[12] D. Yuan, S. Shao, C. Guo, F. Jiang, J. Wang, Grain refining of Ti-6Al-4V alloy fabricated by laser and wire additive manufacturing assisted with ultrasonic vibration, Ultrason. Sonochem. 73 (2021) 105472.
[13] M. Simonelli, D.G. McCartney, P. Barriobero-Vila, N.T. Aboulkhair, Y.Y. Tse, A. Clare, R. Hague, The influence of iron in minimizing the microstructural anisotropy of Ti-6Al-4V produced by laser powder-bed fusion, Metall. Mater. Trans. 51 (5) (2020) 2444–2459.
[14] M. Chen, S. Van Petegem, Z. Zou, M. Simonelli, Y.Y. Tse, C.S.T. Chang, M.G. Makowska, D. Ferreira Sanchez, H. Moens-Van Swygenhoven, Microstructural engineering of a dual-phase Ti-Al-V-Fe alloy via in situ alloying during laser powder bed fusion, Addit. Manuf. 59 (2022) 103173.
[15] F. Huber, T. Papke, C. Scheitler, L. Hanrieder, M. Merklein, M. Schmidt, In situ formation of a metastable β-Ti alloy by laser powder bed fusion (L-PBF) of vanadium and iron modified Ti-6Al-4V, Metals 8 (12) (2018).
[16] J. Allen, An investigation into the comparative costs of additive manufacture vs. machine from solid for aero engine parts, Cost Effective Manufacture via Net-Shape Processing. 17 (2006) 1–17.
[17] E. Alabort, Y.T. Tang, D. Barba, R.C. Reed, Alloys-by-design: a low-modulus titanium alloy for additively manufactured biomedical implants, Acta Mater. 229 (2022) 117749.
[18] X. Chen, C. Qiu, Development of a novel metastable beta titanium alloy with ultrahigh yield strength and good ductility based on laser power bed fusion, Addit. Manuf. 49 (2022) 102501.
[19] C.H. Wang, A.M. Russell, G.H. Cao, A semi-empirical approach to the prediction of deformation behaviors of β-Ti alloys, Scripta Mater. 158 (2019) 62–65.
[20] L. Lilensten, Y. Danard, R. Poulain, R. Guillou, J.M. Joubert, L. Perrière, P. Vermaut, D. Thiaudière, F. Prima, From single phase to dual-phase TRIP-TWIP titanium alloys: design approach and properties, Materialia 12 (2020) 100700.
[21] H. Schwab, F. Palm, U. Kühn, J. Eckert, Microstructure and mechanical properties of the near-beta titanium alloy Ti-5553 processed by selective laser melting, Mater. Des. 105 (2016) 75–80.
[22] H.D. Carlton, K.D. Klein, J.W. Elmer, Evolution of microstructure and mechanical properties of selective laser melted Ti-5Al-5V-5Mo-3Cr after heat treatments, Sci. Technol. Weld. Join. 24 (5) (2019) 465–473.
[23] M.A. Ackers, O.M.D.M. Messé, N. Manninen, O. Stryzhyboroda, U. Hecht, Additive manufacturing of TTFNZ (Ti-4.5Ta-4Fe-7.5Nb-6Zr), a novel metastable β-titanium alloy for advanced engineering applications, J. Alloys Compd. 920 (2022) 165899.
[24] Y. Zhu, K. Zhang, Z. Meng, K. Zhang, P. Hodgson, N. Birbilis, M. Weyland, H.L. Fraser, S.C.V. Lim, H. Peng, R. Yang, H. Wang, A. Huang, Ultrastrong nanotwinned titanium alloys through additive manufacturing, Nat. Mater. 21 (11) (2022) 1258–1262.
[25] R. Duan, S. Li, B. Cai, W. Zhu, F. Ren, M.M. Attallah, A high strength and low modulus metastable β Ti-12Mo-6Zr-2Fe alloy fabricated by laser powder bed fusion in-situ alloying, Addit. Manuf. 37 (2021) 101708.
[26] X. Pang, Z. Xiong, S. Liu, J. Sun, R.D.K. Misra, H. Kokawa, Z. Li, Grain refinement effect of ZrB2 in laser additive manufactured metastable β-titanium alloy with enhanced mechanical properties, Mater. Sci. Eng., A 857 (2022) 144104.
[27] X. Pang, Z. Xiong, C. Yao, J. Sun, R.D.K. Misra, Z. Li, Strength and ductility optimization of laser additive manufactured metastable β titanium alloy by tuning α phase by post heat treatment, Mater. Sci. Eng., A 831 (2022) 142265.
[28] A. Zafari, E.W. Lui, K. Xia, Deformation-free geometric recrystallisation in a metastable β-Ti alloy produced by selective laser melting, Materials Research Letters 8 (3) (2020) 117–122.
[29] D. Li, H. Huang, C. Chen, S. Liu, X. Liu, X. Zhang, K. Zhou, Additive manufacturing of high strength near β titanium alloy Ti-55511 by engineering nanoscale secondary α laths via in-situ heat treatment, Mater. Sci. Eng., A 814 (2021) 141245.
[30] N. Hafeez, J. Liu, L. Wang, D. Wei, Y. Tang, W. Lu, L.-C. Zhang, Superelastic

response of low-modulus porous beta-type Ti-35Nb-2Ta-3Zr alloy fabricated by laser powder bed fusion, Addit. Manuf. 34 (2020) 101264.
[31] R. Ummethala, P.S. Karamched, S. Rathinavelu, N. Singh, A. Aggarwal, K. Sun, E. Ivanov, L. Kollo, I. Okulov, J. Eckert, K.G. Prashanth, Selective laser melting of high-strength, low-modulus Ti–35Nb–7Zr–5Ta alloy, Materialia 14 (2020) 100941.
[32] C. Suwanpreecha, E. Alabort, Y.T. Tang, C. Panwisawas, R.C. Reed, A. Manonukul, A novel low-modulus titanium alloy for biomedical applications: a comparison between selective laser melting and metal injection moulding, Mater. Sci. Eng., A 812 (2021) 141081.
[33] S.L. Sing, Perspectives on additive manufacturing enabled Beta-titanium alloys for biomedical applications, International Journal of Bioprinting 8 (1) (2022).
[34] D. Zhang, D. Qiu, M.A. Gibson, Y. Zheng, H.L. Fraser, D.H. StJohn, M.A. Easton, Additive manufacturing of ultrafine-grained high-strength titanium alloys, Nature 576 (7785) (2019) 91–95.
[35] C. Zhang, X. Bao, M. Hao, W. Chen, D. Zhang, D. Wang, J. Zhang, G. Liu, J. Sun, Hierarchical nano-martensite-engineered a low-cost ultra-strong and ductile titanium alloy, Nat. Commun. 13 (1) (2022) 5966.
[36] S.M. Market, Shanghai metals market, https://www.metal.com/. (Accessed 21 March 2024).
[37] L.M. Exchange, London Metal Exchange. https://www.lme.com/en/. (Accessed 2024/March/21.
[38] M.O. Bodunrin, L.H. Chown, J.A. Omotoyinbo, Development of low-cost titanium alloys: a chronicle of challenges and opportunities, Mater. Today: Proc. 38 (2021) 564–569.
[39] P.J. Bania, Beta titanium alloys and their role in the titanium industry, J. Occup. Med. 46 (7) (1994) 16–19.
[40] R.P. Kolli, W.J. Joost, S. Ankem, Phase stability and stress-induced transformations in beta titanium alloys, J. Occup. Med. 67 (6) (2015) 1273–1280.
[41] S.A. Mantri, M.S.K.K.Y. Nartu, S. Dasari, A. Sharma, P. Agrawal, R. Salloom, F. Sun, E. Ivanov, K. Cho, B. McWilliams, S.G. Srinivasan, N.B. Dahotre, F. Prima, R. Banerjee, Suppression and reactivation of transformation and twinning induced plasticity in laser powder bed fusion additively manufactured Ti-10V-2Fe-3Al, Addit. Manuf. 48 (2021) 102406.
[42] C. Qiu, Q. Liu, R. Ding, Significant enhancement in yield strength for a metastable beta titanium alloy by selective laser melting, Mater. Sci. Eng., A 816 (2021) 141291.
[43] I. Weiss, S.L. Semiatin, Thermomechanical processing of beta titanium alloys—an overview, Mater. Sci. Eng., A 243 (1) (1998) 46–65.
[44] S. Neelakantan, P.E.J. Rivera-Díaz-del-Castillo, S. van der Zwaag, Prediction of the martensite start temperature for β titanium alloys as a function of composition, Scripta Mater. 60 (8) (2009) 611–614.
[45] P. Konda Gokuldoss, Design of next-generation alloys for additive manufacturing, Material Design & Processing Communications 1 (4) (2019) e50.
[46] J. Ballor, T. Li, F. Prima, C.J. Boehlert, A. Devaraj, A review of the metastable omega phase in beta titanium alloys: the phase transformation mechanisms and its effect on mechanical properties, Int. Mater. Rev. 68 (1) (2023) 26–45.
[47] P. Evans, Twinning-induced Plasticity in Metastable Beta Titanium Alloys, Imperial College London, 2017.
[48] N. Okano, Y. Shinohara, Y. Kusano, M. Tahara, T. Inamura, S. Miyazaki, H. Hosoda, Effect of Sn content on phase constitution and mechanical properties of Ti-Cr-Sn shape memory alloys, Mater. Today: Proc. 2 (2015) S825–S828.
[49] B. Vrancken, L. Thijs, J.P. Kruth, J. Van Humbeeck, Microstructure and mechanical properties of a novel β titanium metallic composite by selective laser melting, Acta Mater. 68 (2014) 150–158.
[50] Q. Wang, C. Han, T. Choma, Q. Wei, C. Yan, B. Song, Y. Shi, Effect of Nb content on microstructure, property and in vitro apatite-forming capability of Ti-Nb alloys fabricated via selective laser melting, Mater. Des. 126 (2017) 268–277.
[51] W. Chen, C. Chen, X. Zi, X. Cheng, X. Zhang, Y.C. Lin, K. Zhou, Controlling the microstructure and mechanical properties of a metastable β titanium alloy by selective laser melting, Mater. Sci. Eng., A 726 (2018) 240–250.
[52] Y.J. Liu, Y.S. Zhang, L.C. Zhang, Transformation-induced plasticity and high strength in beta titanium alloy manufactured by selective laser melting, Materialia 6 (2019) 100299.
[53] C. Qiu, Q. Liu, Multi-scale microstructural development and mechanical properties of a selectively laser melted beta titanium alloy, Addit. Manuf. 30 (2019) 100893.
[54] N. Hafeez, D. Wei, L. Xie, Y. Tang, J. Liu, H. Kato, W. Lu, L.-C. Zhang, L. Wang, Evolution of microstructural complex transitions in low-modulus β-type Ti-35Nb-2Ta-3Zr alloy manufactured by laser powder bed fusion, Addit. Manuf. 48 (2021) 102376.
[55] A. Takase, T. Ishimoto, R. Suganuma, T. Nakano, Surface residual stress and phase stability in unstable β-type Ti–15Mo–5Zr–3Al alloy manufactured by laser and electron beam powder bed fusion technologies, Addit. Manuf. 47 (2021) 102257.
[56] C. Schulze, M. Weinmann, C. Schweigel, O. Keßler, R. Bader, Mechanical properties of a newly additive manufactured implant material based on Ti-42Nb, Materials 11 (1) (2018) 124.
[57] M.A. Macias-Sifuentes, C. Xu, O. Sanchez-Mata, S.Y. Kwon, S.E. Atabay, J.A. Muñiz-Lerma, M. Brochu, Microstructure and mechanical properties of β-21S Ti alloy fabricated through laser powder bed fusion, Progress in Additive Manufacturing 6 (3) (2021) 417–430.
[58] F.F. Ahmed, S.J. Clark, C.L. Alex Leung, L. Stanger, J. Willmott, S. Marussi, V. Honkimaki, N. Haynes, H.S. Zurob, P.D. Lee, A.B. Phillion, Achieving homogeneity in a high-Fe β-Ti alloy laser-printed from blended elemental powders, Mater. Des. 210 (2021) 110072.
[59] D.N. Williams, Using electron/atom ratio in titanium alloy design, J. Mater. Sci. 10 (7) (1975) 1239–1241.
[60] D. Kuroda, M. Niinomi, M. Morinaga, Y. Kato, T. Yashiro, Design and mechanical properties of new β type titanium alloys for implant materials, Mater. Sci. Eng., A 243 (1) (1998) 244–249.
[61] M. Abdel-Hady, K. Hinoshita, M. Morinaga, General approach to phase stability and elastic properties of β-type Ti-alloys using electronic parameters, Scripta Mater. 55 (5) (2006) 477–480.
[62] M. Morinaga, N. Yukawa, T. Maya, K. Sone, H. Adachi, Theoretical design of titanium alloys, Sixth World Conference on Titanium III (1988) 1601–1606.
[63] C. Brozek, F. Sun, P. Vermaut, Y. Millet, A. Lenain, D. Embury, P.J. Jacques, F. Prima, A β-titanium alloy with extra high strain-hardening rate: design and mechanical properties, Scripta Mater. 114 (2016) 60–64.
[64] C.A.R.P. Baptista, S.G. Schneider, E.B. Taddei, H.M. da Silva, Fatigue behavior of arc melted Ti–13Nb–13Zr alloy, Int. J. Fatig. 26 (9) (2004) 967–973.
[65] A.A. Martin, N.P. Calta, S.A. Khairallah, J. Wang, P.J. Depond, A.Y. Fong, V. Thampy, G.M. Guss, A.M. Kiss, K.H. Stone, C.J. Tassone, J. Nelson Weker, M.F. Toney, T. van Buuren, M.J. Matthews, Dynamics of pore formation during laser powder bed fusion additive manufacturing, Nat. Commun. 10 (1) (2019) 1987.
[66] K.G. Prashanth, S. Scudino, T. Maity, J. Das, J. Eckert, Is the energy density a reliable parameter for materials synthesis by selective laser melting? Materials Research Letters (2017) 1–5.
[67] L.M. Gammon, R.D. Briggs, J.M. Packard, K.W. Batson, R. Boyer, C.W. Domby, Metallography and microstructures of titanium and its alloys, ASM handbook 9 (2004) 899–917.
[68] M.S. Park, W.-T. Chiu, N. Nohira, M. Tahara, H. Hosoda, Effects of Cr and Sn additives on the martensitic transformation and deformation behavior of Ti-Cr-Sn biomedical shape memory alloys, Mater. Sci. Eng., A 822 (2021) 141668.
[69] E. Bertrand, P. Castany, I. Péron, T. Gloriant, Twinning system selection in a metastable β-titanium alloy by Schmid factor analysis, Scripta Mater. 64 (12) (2011) 1110–1113.
[70] G. Lütjering, J.C. Williams, Titanium, Springer Science & Business Media, 2007.
[71] H. Tobe, H.Y. Kim, T. Inamura, H. Hosoda, S. Miyazaki, Origin of {332} twinning in metastable β-Ti alloys, Acta Mater. 64 (2014) 345–355.
[72] J. Gao, Y. Huang, D. Guan, A.J. Knowles, L. Ma, D. Dye, W.M. Rainforth, Deformation mechanisms in a metastable beta titanium twinning induced plasticity alloy with high yield strength and high strain hardening rate, Acta Mater. 152 (2018) 301–314.
[73] G. Welsch, R. Boyer, E. Collings, Materials Properties Handbook: Titanium Alloys, ASM international, 1993.
[74] F. Sun, J.Y. Zhang, M. Marteleur, T. Gloriant, P. Vermaut, D. Laillé, P. Castany, C. Curfs, P.J. Jacques, F. Prima, Investigation of early stage deformation mechanisms in a metastable β titanium alloy showing combined twinning-induced plasticity and transformation-induced plasticity effects, Acta Mater. 61 (17) (2013) 6406–6417.
[75] S.A. Mantri, F. Sun, D. Choudhuri, T. Alam, B. Gwalani, F. Prima, R. Banerjee, Deformation induced hierarchical twinning coupled with omega transformation in a metastable β-Ti alloy, Sci. Rep. 9 (1) (2019) 1334.
[76] J.M. Oh, C.H. Park, J.-T. Yeom, J.-K. Hong, N. Kang, S.W. Lee, High strength and ductility in low-cost Ti–Al–Fe–Mn alloy exhibiting transformation-induced plasticity, Mater. Sci. Eng., A 772 (2020) 138813.
[77] H. Okamoto, Sn-Ti (Tin-Titanium), J. Phase Equilibria Diffus. 31 (2) (2010) 202–203.
[78] A. Wadood, T. Inamura, H. Hosoda, S. Miyazaki, Comparative study of Ti-xCr-3Sn alloys for biomedical applications, Mater. Trans. 52 (9) (2011) 1787–1793.
[79] X. Min, X. Chen, S. Emura, K. Tsuchiya, Mechanism of twinning-induced plasticity in β-type Ti–15Mo alloy, Scripta Mater. 69 (5) (2013) 393–396.
[80] M.J. Lai, C.C. Tasan, D. Raabe, On the mechanism of {332} twinning in metastable β titanium alloys, Acta Mater. 111 (2016) 173–186.
[81] M. Bignon, E. Bertrand, F. Tancret, P.E.J. Rivera-Díaz-del-Castillo, Modelling martensitic transformation in titanium alloys: the influence of temperature and deformation, Materialia 7 (2019) 100382.
[82] P.C. Collins, D.A. Brice, P. Samimi, I. Ghamarian, H.L. Fraser, Microstructural control of additively manufactured metallic materials, Annu. Rev. Mater. Res. 46 (1) (2016) 63–91.
[83] G. Zhang, J. Chen, M. Zheng, Z. Yan, X. Lu, X. Lin, W. Huang, Element vaporization of Ti-6Al-4V alloy during selective laser melting, Metals 10 (4) (2020) 435.
[84] P.A. Hooper, Melt pool temperature and cooling rates in laser powder bed fusion, Addit. Manuf. 22 (2018) 548–559.
[85] C. Yaws, The Yaws Handbook of Vapor Pressure: Antoine Coefficients, Gulf Professional Publishing, 2015.
[86] A. Block-Bolten, T.W. Eagar, Selective evaporation of metals from weld pools, Trends in welding research in the United States (1982) 53–73.
[87] S.L. Semiatin, V.G. Ivanchenko, O.M. Ivasishin, Diffusion models for evaporation losses during electron-beam melting of alpha/beta-titanium alloys, Metall. Mater. Trans. B 35 (2) (2004) 235–245.